Hindawi Publishing Corporation
International Journal of Aerospace Engineering
Volume 2016, Article ID 5396876, 12 pages
http://dx.doi.org/10.1155/2016/5396876

Research Article

Study on Helicopter Antitorque Device Based on Cross-Flow Fan Technology

Du Siliang, Tang Zhengfei, Xu Pei, and Ji Mengjiang

National Key Laboratory of Science and Technology on Rotorcraft Aeromechanics, Nanjing University of Aeronautics and Astronautics, Nanjing 210016, China

Correspondence should be addressed to Du Siliang; kjofchina@qq.com

Received 8 June 2016; Revised 17 October 2016; Accepted 2 November 2016

Academic Editor: Maria G. De Giorgi

In order to improve low-altitude flight security of single-rotor helicopter, an experimental model of a helicopter antitorque device is developed for wind tunnel test. The model is based on the flow control technology of the cross-flow fan (CFF). Wind tunnel tests show that the model can produce side force. It is concluded that the influence of the CFF rotating speed, the rotor collective pitch, and the forward flight speed on the side force of the model is great. At the same time, the numerical simulation calculation method of the model has been established. Good agreement between experimental and numerical side force and power shows that results of numerical solution are reliable. Therefore, the results in actual helicopter obtained from Computational Fluid Dynamics (CFD) solution are acceptable. This proves that this antitorque device can be used for a helicopter.

1. Introduction

The basic advantage of the conventional tail rotors is that they require relatively little power, produce good yaw control, and contribute significantly to yaw damping and directional stability in forward flight [1]. Against these good features are the bad ones [2]: a tail rotor is dangerous to people on the ground and to itself if swung into trees, fence posts, or wires. Large helicopters circumvent these problems by incorporating tail rotors that are well above the ground, but the exposed whirling blades on smaller rotorcraft may be perceived as dangerous enough to prompt the consideration of another system. Some helicopter designs balance the main-rotor torque by using two or more rotors, while other designs eliminate the torque, applying a tip-jet drive concept. But the torque from a single shaft driven main rotor that is offset by a tail rotor is still the main direction of development of the helicopter. At present, the antitorque system is more mature with the tail rotor, the fenestron [3, 4], and no tail rotor (NOTAR) concept [5–10]. They all have some advantages or disadvantages. As with the tail rotor, the larger the diameter of the fenestron, the less the power it takes from the engine. However, in order to reduce the weight of the duct, the fenestron fan diameter can be as small as 50% of the tail rotor. Thus, it uses more power for antitorque than a typical tail rotor, taking power which could be used by the main rotor. To be effective, the depth of the duct should be at least 20% of the fan diameter, according to the theory. This means that it is difficult to streamline the thick fan for low drag in forward flight. This also means that the air path into and out of the fan is tortuous, so its efficiency is penalized. Another antitorque system to eliminate the tail rotor is the Hughes NOTAR. The system uses a variable pitch fan inside the tail boom to build a high volume of low-pressure air, which exits through two slots and creates a boundary layer flow of air along the tail boom utilizing the Coanda effect. The boundary layer changes the direction of airflow around the tail boom, creating thrust opposite the motion imparted to the fuselage by the torque effect of the main rotor. Benefits of the NOTAR system include increased safety (the tail rotor being vulnerable) and greatly reduced external noise. However, compared to the tail rotor, NOTAR is not widely used for reasons of low effective rate, weak maneuverability, and patent constraints. As for these bad factors, a new antitorque device, which can control flow with the assistance from the CFF, has been proposed. The CFF has been used in aircraft propulsion and flow control recently. The fan-wing aircraft [11–16] is one of them. Fan-wing aircraft makes use of a CFF to accelerate oncoming

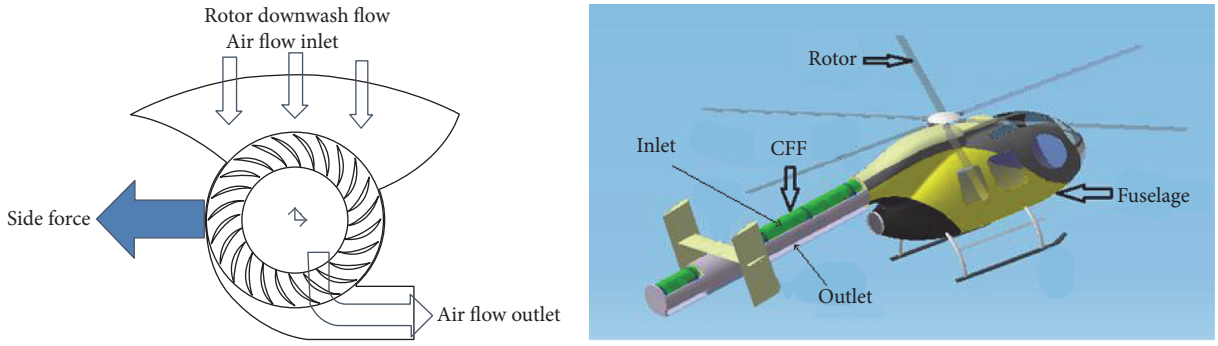

(a) Principle of side force generation

(b) The installation position of the antitorque device

Figure 1: Schematic diagram of CFF antitorque device.

airflow over a relatively thick aerofoil section, producing lift and thrust simultaneously. The advantages of fan-wing aircraft compared to the conventional aircrafts are short take-off and landing (STOL) at the low forward speed, no stall, and high power load. Another one using CFF is the propulsive wing [17, 18], which embeds a CFF into a thick wing for both lift enhancement and thrust production. It has the same advantages as fan-wing aircraft. There are also vertical take-off and landing (VTOL) aircraft using the CFF proposed by Gossett. It may be a good choice to use the CFF in helicopter antitorque system due to its advantages [19, 20].

A new antitorque system should have a little impact on helicopter aerodynamic characteristics to avoid complex dynamic phenomena such as the aerodynamic coupling with other components of the helicopter, reduce the aerodynamic noise, and avoid the aerodynamic force which is difficult to control. Finally, the antitorque system should be easy to operate and control. The aim of the present work is to build and test an antitorque device and to use CFF and verify that it has the ability to produce side force. It is also necessary to analyze the relationship with the side force and power by changing the rotating speed, the rotor collective pitch, and the forward flight speed. In order to simulate and analyze the aerodynamic characteristics of the device in a real helicopter, it is necessary to establish a CFD method, the results of which are validated with the experimental data presented in wind tunnel test.

2. Experimental Method

2.1. Wind Tunnel and Model Arrangements. The CFF consists of a drum-like rotor with forward curved blades, encased within housing walls. The inlet and outlet have rectangular cross sections. The advantage of CFF is its ability to extend lengthwise, producing a uniformly distributed inflow and outflow and approximately 90° flow turning from the inlet to the outlet. Therefore, the antitorque device we proposed is shown in Figure 1(a). Figure 1(b) illustrates the principle sketch of the antitorque device embedded in tail boom with MD600 fuselage.

This experiment is based on the low speed open return flow wind tunnel (Figure 2(a)), which is made by the National Key Laboratory of Rotorcraft Aeromechanics in Nanjing University of Aeronautics and Astronautics. The basic parameters of the experimental wind tunnel are shown in Table 1. Figure 2(b) shows the geometric parameters of the experimental antitorque device model. The experimental model is shown in Figure 2(c). The left interface and the right interface of the model can be separately removed, and the parameters are defined in Table 2. The whole experimental bench is placed in the relative position of the wind tunnel as shown in Figure 2(d). The basic parameters of the rotor used in the experiment are shown in Table 3. As the rotor thrust will change in different flows in wind tunnel, this article used rotor collective pitch to define the rotor downwash effects. Table 4 shows that when the rotor rotation speed is 900 r/min, rotor thrust changes with the collective pitch at different forward flight speed. The six-component balance was used in the experiment (Figure 2(e)).

Table 1: Parameters of wind tunnel.

Parameters	Value
Size of test area (m × m)	3.4 × 2.4
Maximum wind speed (m/s)	40
Minimum stable wind speed (m/s)	5
Shrinkage ratio	4

Table 2: Definitions of geometric parameters.

Definition	Value
Opening angle ψ (°)	90, 110, 130, 150
Outer radius of CFF $R1$ (mm)	100
Fan outlet height ζ (mm)	45
Blade mounting angle γ (°)	0, 10, 20, 30
Blade chord C (mm)	25
Number of blades (piece)	10, 12, 14, 16
Blade length (mm)	500
Clearance between CFF and shell σ (mm)	5

2.2. Experimental Method. The experiment includes three states, namely, static state, hover state, and forward flight state. Static state experiments are defined as the antitorque device has no rotor downwash flow and static forward flight

(a) Wind tunnel

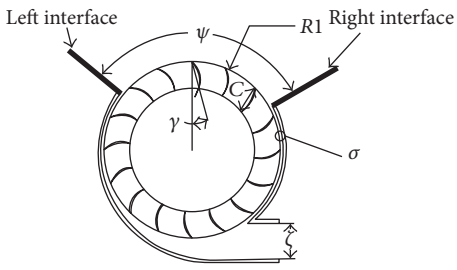

(b) Definition of section geometry parameters

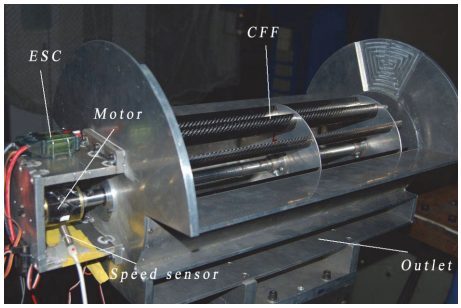

(c) Experimental model

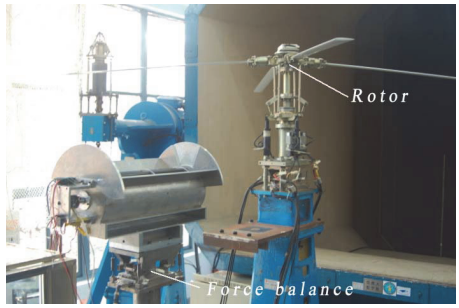

(d) The position of the experimental model in wind tunnel

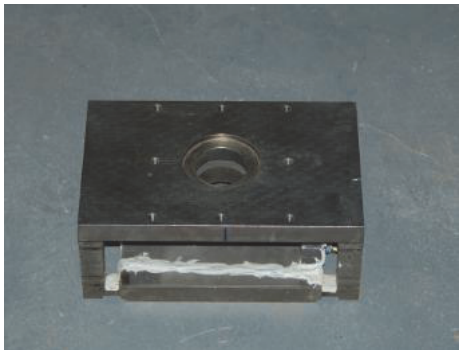

(e) Six-component balance

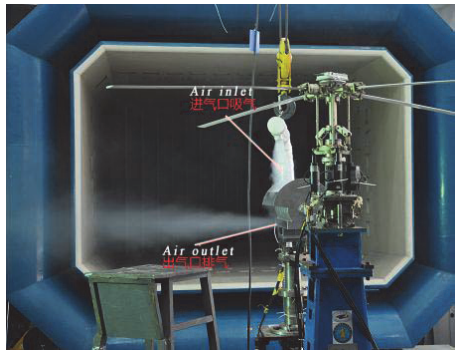

(f) Principle verification

Figure 2: Experimental model and equipment.

Table 3: Parameters of rotor test bench.

Parameters	Value
Number of blades (piece)	4
Blade radius (m)	1.25
Blade chord (m)	0.072
Geometric torsion (°)	0
Rotor solidity	0.077
Blade airfoil	NACA 0012

Table 4: Lift of rotor in wind tunnel test.

Free stream velocity (m/s)	0			5			10		
Collective pitch (°)	8	10	12	8	10	12	8	10	12
Rotor lift (kg)	35	45	59	37	49	62	41	53	65

inflow. The hover state experiment is defined as the antitorque device is in the rotor downwash flow, without the forward flight inflow. The forward flight state experiment is defined as the antitorque device is in the rotor downwash flow and forward flight inflow. First of all, the principle experiment of the side force generation has been carried out in static state. A smoke generator was placed on the top of the model. CFF rotational speed is set through the controller (Figure 3). Smoke billowed out from the model outlet (Figure 2(f)). This proved that the model can produce 90° flow turning from inlet to the outlet. So, it can generate a force in the opposite direction of the jet. The force data of the balance was collected and processed by a computer (data acquisition speed is 100 KHz).

2.3. Measurement Uncertainty. The experimental uncertainty is mostly expressed as fractional uncertainty of the measured value (Table 5). All measurement uncertainties were estimated from systematic and random sources of error that

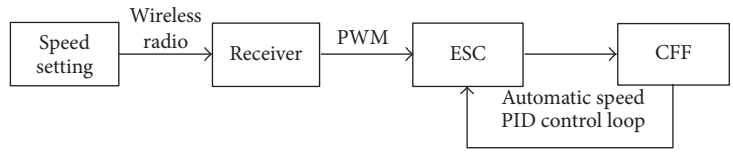

Figure 3: Control block diagram of the rotation speed of CFF.

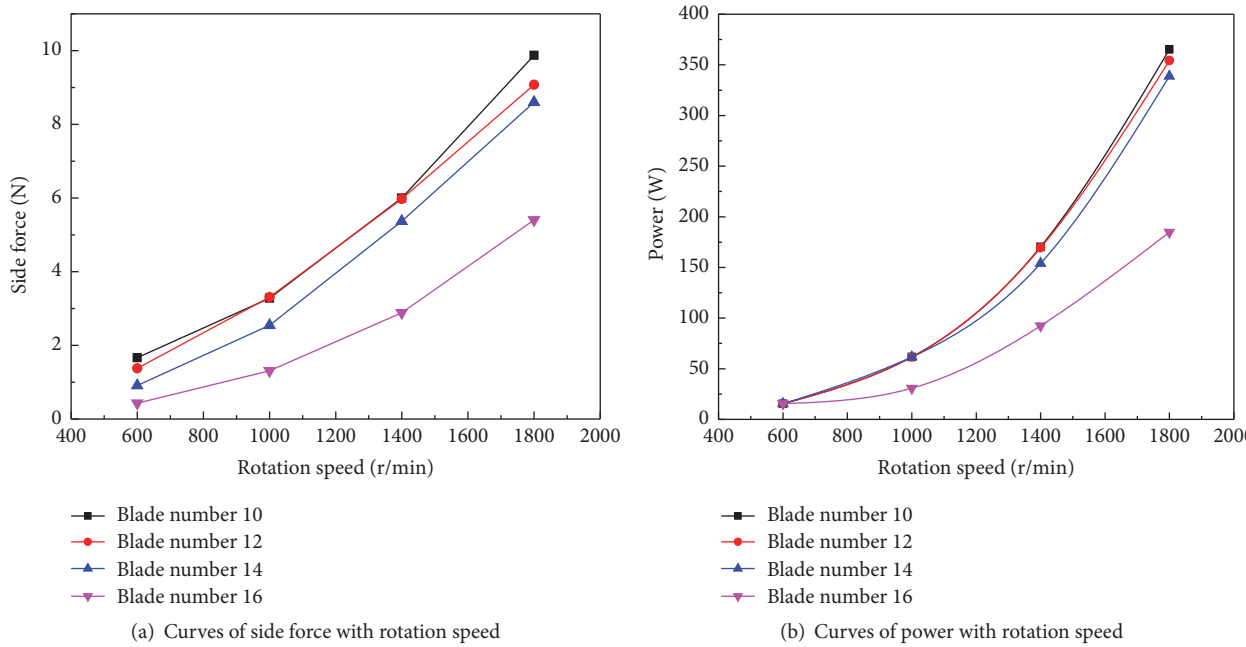

(a) Curves of side force with rotation speed

(b) Curves of power with rotation speed

Figure 4: Influence of blade number.

Table 5: Summary of the measurement uncertainties.

Parameters	Uncertainty
Force balance (kg)	±0.03%
Data acquisition resolution	±0.05%
Free stream velocity (m/s)	±0.5%
Free stream deflection angle (°)	±0.1%
Model installation angle (°)	±1%
Rotor collective pitch angle (°)	±1%

included the instrument calibration, instrument accuracy given by the manufacturer, and the data acquisition resolution.

3. Experimental Results and Analysis

3.1. Static State

3.1.1. Influence of Blade Number. Figure 4(a) shows the relationship between side force and rotation speed at different blade numbers when the blade installation angle is 10 degrees, with both interfaces, and the opening angle is 110 degrees in Figure 4(a). It can be figured out that the side force increases as the rotational speed increases and the increase rate is progressively larger with a rising trend. This means the rotation speed of CFF has a great influence on the side force. The higher the speed, the larger the side force. From the figure, we can find that the side force is greater with fewer blades, and when the number of the blades is less than 14 pieces, the increasing amount changes a little at different rotation speeds. Figure 4(b) shows the relationship between required power and rotational speed in different blade numbers. The faster the rotating speed of the CFF, the higher the power consumption. At the same rotational speed, the fewer the number of blades, the higher the power consumption. When the number of the blades is less than 14 pieces, the power consumption of the same speed is basically the same. When the blade number is 10 pieces, the maximum power load is 2.71 kg/kw (1800 r/min).

3.1.2. Influence of Blade Mounting Angle. Figure 5(a) shows the relationship between side force and rotational speed with different blade mounting angles when the blade number is 12 pieces, with both interfaces, and the opening angle is 110 degrees. It can be seen that the side force obviously increases as the rotational speed of the cross-flow fan increases. The higher the speed, the more obvious the side force increases. At high speed, the side force is different with the change of the angle of installation. From the figure, we can see that when the blade mounting angle is 20 degrees, it has a higher side force at the same speed compared with the other mounting

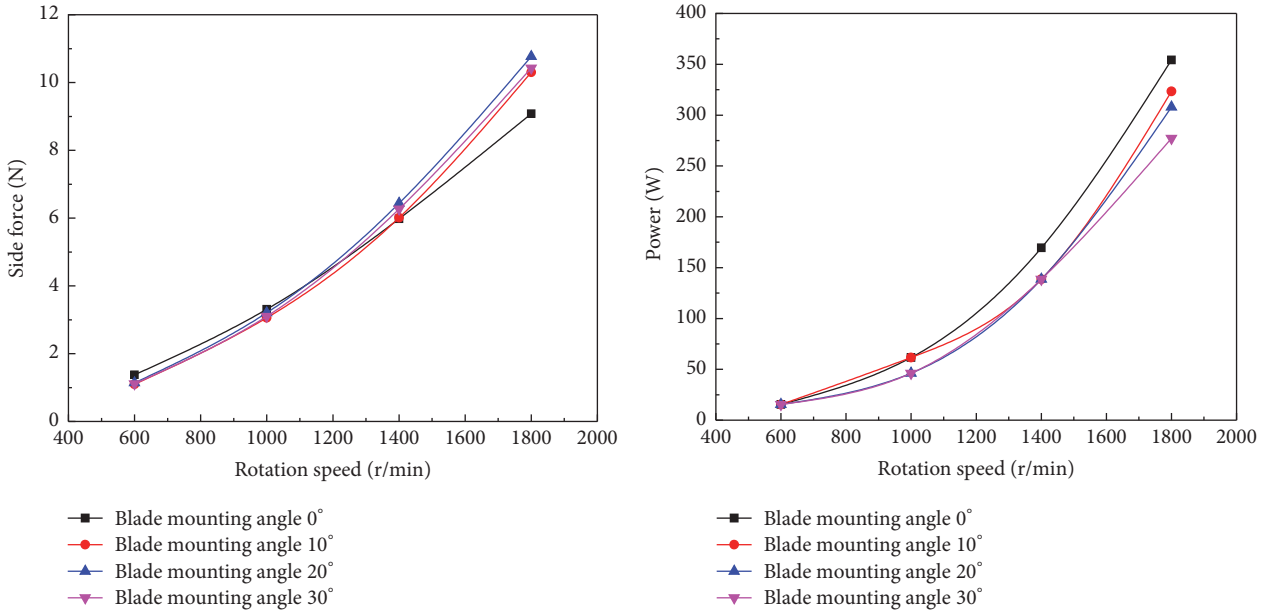

(a) Curves of lateral force with rotation speed

(b) Curves of power with rotation speed

Figure 5: Influence of blade mounting angle.

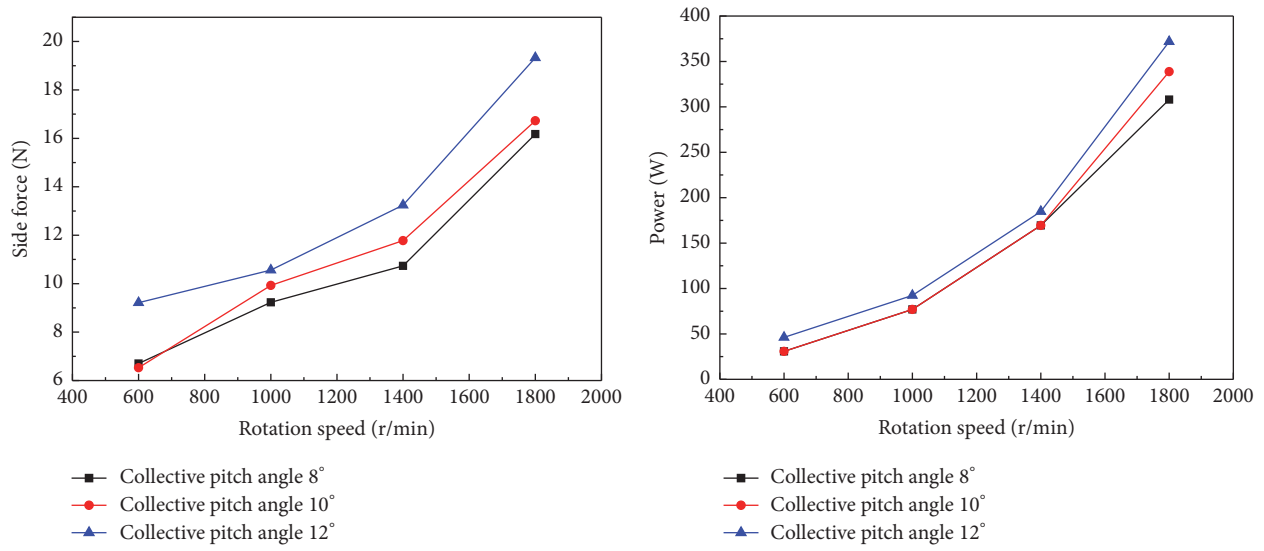

(a) Curves of side force with rotation speed

(b) Curves of power with rotation speed

Figure 6: Hover state.

angle. Figure 5(b) shows the relationship between power required and rotation speed with different blade mounting angles. Compared with Figure 5(a), it can be seen that when the rotation speed is 1800 r/min and the blade mounting angle is 20 degrees, the power load is max and is equal to 3.50 kg/kw.

3.2. Hover State. Figure 6(a) shows the relationship between side force and rotational speed with different rotor collective pitches when the blade number is 12 pieces, blade mounting angle is 20 degrees, with both interfaces, and the opening angle is 110 degrees. It can be seen from the chart that the greater the rotor collective pitch, the greater the side force, which means the rotor downwash flow has a significant impact on the side force of the antitorque device. Side force is large (equal to 19.32 N) when the CFF rotation speed is 1800 r/min and the rotor collective pitch is 12 degrees. The side force increased by about 80% compared with the maximum value of 10.76 N in Figure 4(a) (with no downwash flow). Figure 6(b) shows the relationship between required power of antitorque device and the rotation speed of CFF. Compared with Figure 5(b), when rotor downwash flow exists, with the same rotation speed of CFF, the required power of reactive torque device is higher than that of the

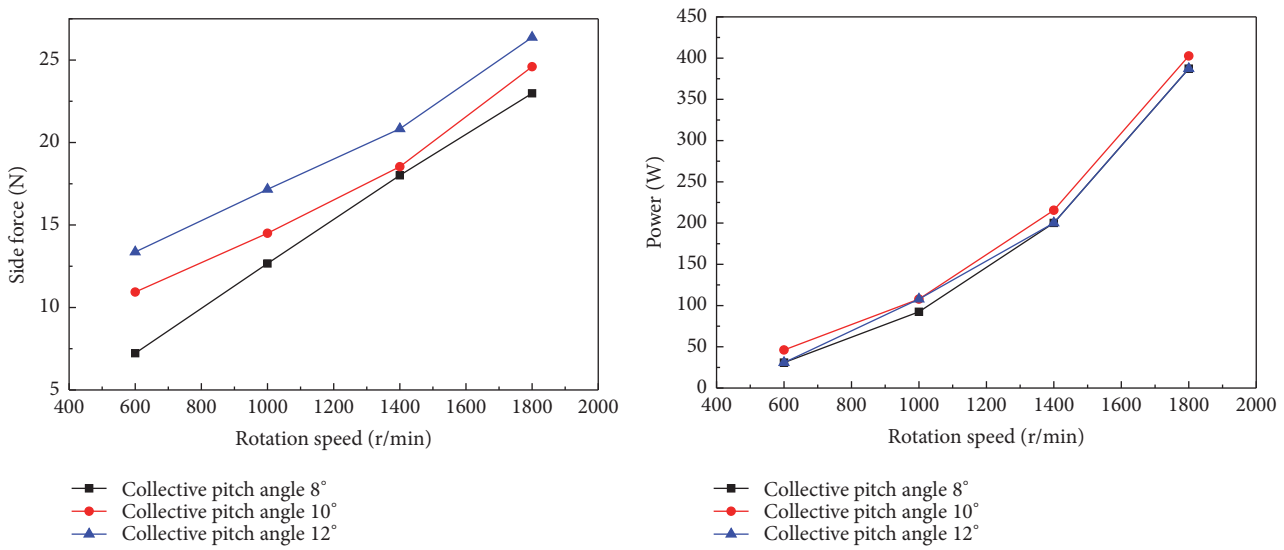

(a) Curves of side force with rotation speed

(b) Curves of power with rotation speed

Figure 7: Forward flight speed is 5 m/s.

static state. The maximum power load is 5.20 kg/kw, when the rotation speed is 1800 r/min.

3.3. Forward Flight State

3.3.1. Forward Flight Speed Is 5 m/s. Figure 7(a) shows the relationship between side force and rotational speed with different rotor collective pitches when the blade number is 12 pieces, blade mounting angle is 20 degrees, with both interfaces, the opening angle is 110 degrees, and forward speed is 5 m/s. As can be seen from the figure, the side force increases as the rotational speed increases and also increases with the rotor collective pitch. In contrast to Figure 6(a), it is shown that the side force produced by antitorque device when forward flight flow exists is larger than that without forward flight flow. Figure 7(b) shows the relationship between power and the rotation speed of CFF with different rotor collective pitches when the forward speed is 5 m/s. It can be found from the figure that the power consumption changes a little at the same rotation speed. It can be inferred that there is a part of the forward flight airflow under the effect of rotor downwash rushing into the cross-flow fan of the antitorque device, thereby increasing the side force.

3.3.2. Forward Flight Speed Is 10 m/s. Figure 8(a) shows the relationship between side force and rotational speed with different rotor collective pitches when the blade number is 12 pieces, blade mounting angle is 20 degrees, with an interface, the opening angle is 110 degrees, and forward speed is 5 m/s. Compared with Figure 15, we can find that when the rotor collective pitch and the rotation speed are the same, the side force increases more obviously when the forward speed is large. Figure 8(b) shows the power change curve. It shows that power changes a little at the same rotation speed and collective pitch and proves that the forward flight airflow under the effect of rotor downwash rushes into the CFF of the antitorque device. The maximum power load of 0 m/s, 5 m/s, and 10 m/s is 5.20 kg/kw, 6.94 kg/kw, and 7.45 kg/kw (rotor collective pitch 12 degrees, CFF rotation speed 1800 r/min). Therefore, the forward flow has the role of unloading on the antitorque device, which means when the helicopter needs certain reactive torque, the higher the flight speed, the lower the power consumption.

4. Numerical Methods and Comparison

4.1. Numerical Calculation Method. The numerical simulations are performed using the commercial general-purpose CFD code FLUENT 14.5 by Fluent Inc. The ANSYS ICEM software was used for grid division. Numerical calculation results will be compared with the experimental data. A two-domain model for the numerical calculation is shown in Figure 9. For this CFD analysis, the rotation speed of the fan varies between 400 and 1200 r/min, free stream velocity is 5 m/s, and angle of attack is zero. Free stream velocity and angle of attack are constant for all rotation velocities. Renormalization group (RNG) k-ε model was used for turbulence. The pressure-velocity coupling was calculated using the SIMPLEC algorithm. Second-order upwind discretization was considered for the convection terms. Finite volume method with rectangular elements was used for the whole solution domain. The rotating and stationary domains connected each other with a fluid-fluid interface, where the flow continuity is satisfied (Figure 9(a)). To simulate the fan rotation, the area surrounding the blades was designed as a sliding mesh region (Figure 9(b)). The dimensions of the computational box are 30 $R1$ × 20 $R1$. A uniform velocity is imposed at the inlet, while a zero relative static pressure is prescribed at the outlet. Unsteady simulations require proper setting of both the time step size and the convergence criteria within each time step. For this simulation, a time step size equal to 1/20th the blade passing period captured the unsteady flow

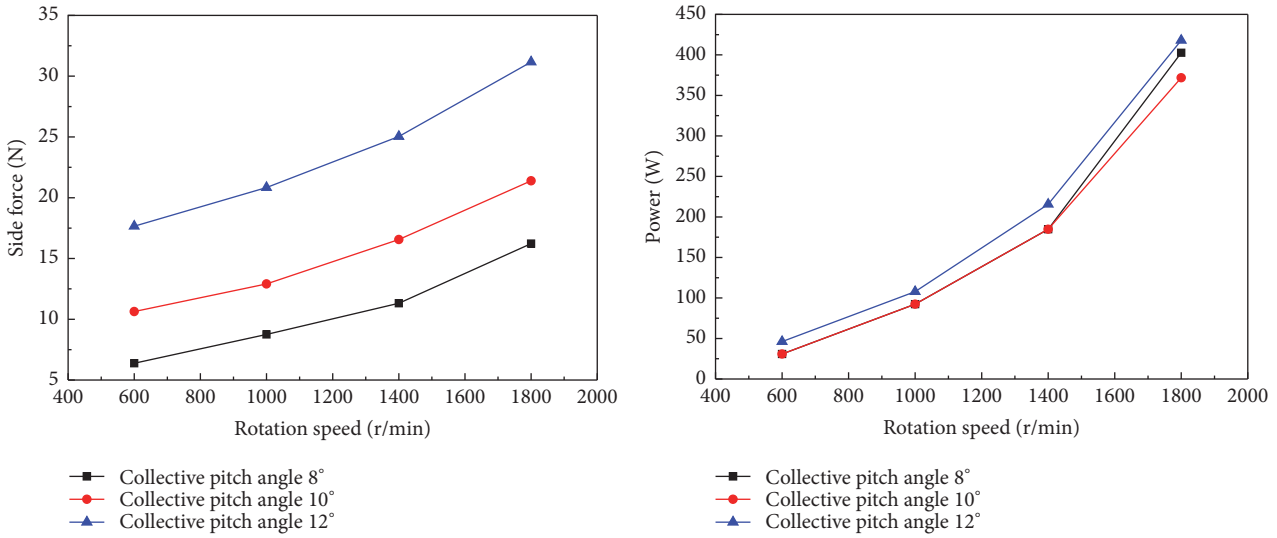

(a) Curves of side force with rotation speed

(b) Curves of power with rotation speed

Figure 8: Forward flight speed is 10 m/s.

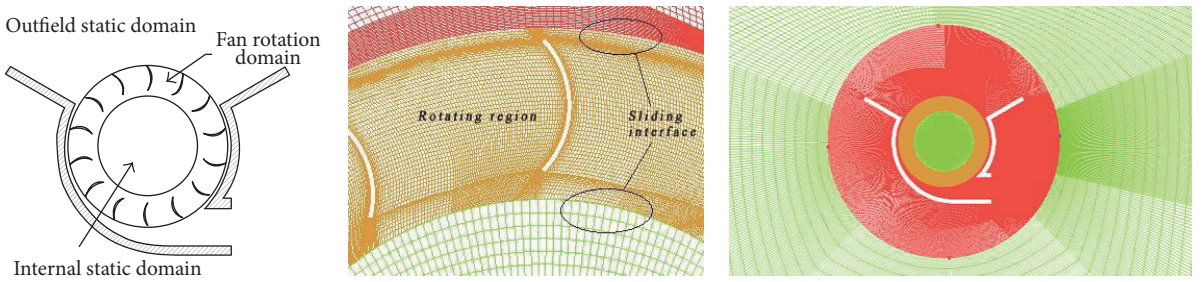

(a) Calculation domain definition

(b) Interface definition

(c) Mesh generation complete

Figure 9: Computational grid generation.

well. Within each time step, iterations were performed until the solution no longer changed. It was found to be necessary to reduce all residuals to at least 10^{-5}. Figure 9(c) shows the mesh generation complete.

4.2. Grid Convergence. There is measurement uncertainty in the experiments and numerical convergence in simulation: purely two-dimensional simulation in CFD and three-dimensionality of flow near the wing ends in the experiment, with inevitable mechanical losses in experiment but not in CFD. Domain size influence has been checked by extending the domain in each direction by an additional 50 per cent in length, respectively. Results (in terms of the side force) agree well with those from the baseline domain, confirming that the size of the current domain is large enough for an accurate prediction.

Grid independency studies were also conducted with three successive grids: coarse, medium, and fine meshes. The coarse mesh has 368,632 elements in total without any inflation layer near the walls. The medium mesh has 599,146 elements with a small element cluster around the blades and the central area. The inflation layer of 1 mm from the first element to the wall is added to both housing and shaft walls. The fine mesh has 1,163,316 elements with more strict mesh controls at the same locations as those used in the medium mesh. In particular, the inflation height is decreased considerably from 1 mm down to 0.1 mm. The study has shown that differences in results from the coarse and medium meshes are significant, while differences in results between the medium and fine meshes are almost negligible. Hence, it is decided to use the medium mesh as the baseline for further simulation.

4.3. Static State Comparison

4.3.1. Blade Mounting Angle Is 10 Degrees. Figure 10 shows numerical simulation calculation and test results contrast curve when blade number is 16, blade installation angle is 10 degrees, with both interfaces, and opening angle is 110 degrees. We can see that there is a little difference between the results of numerical simulation and the experimental results in the error range, and the tendency is consistent. This means the numerical calculation method for the side force and the required power of the reactive torque device is credible.

4.3.2. Blade Mounting Angle Is 20 Degrees. Figure 11 shows numerical simulation calculation and test results contrast

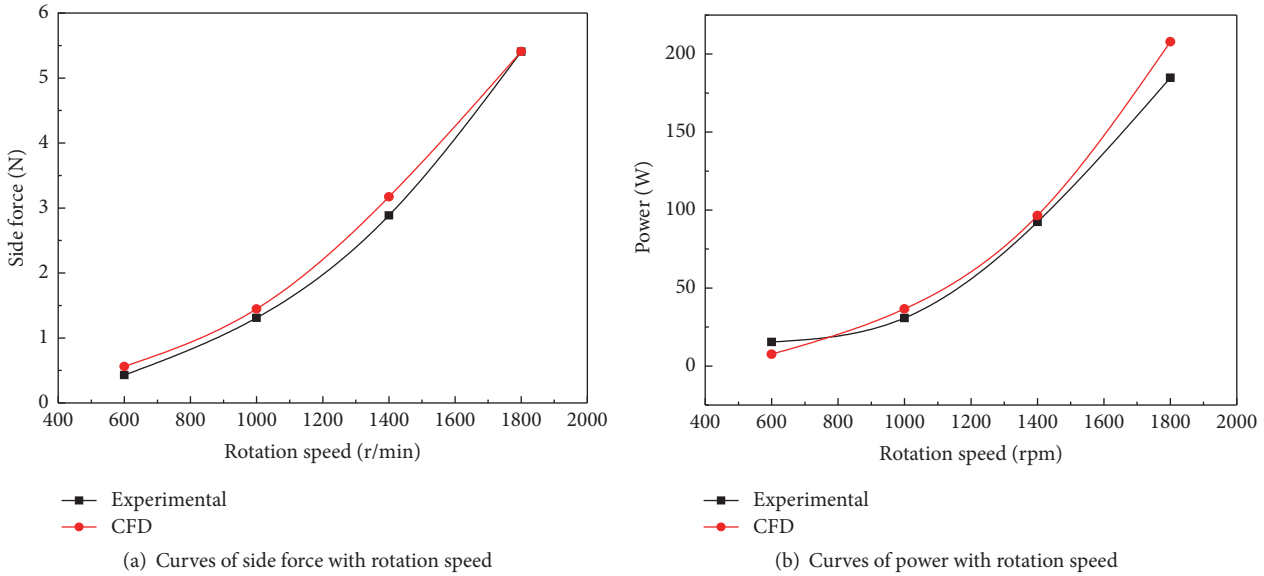

(a) Curves of side force with rotation speed

(b) Curves of power with rotation speed

Figure 10: Blade mounting angle is 10 degrees.

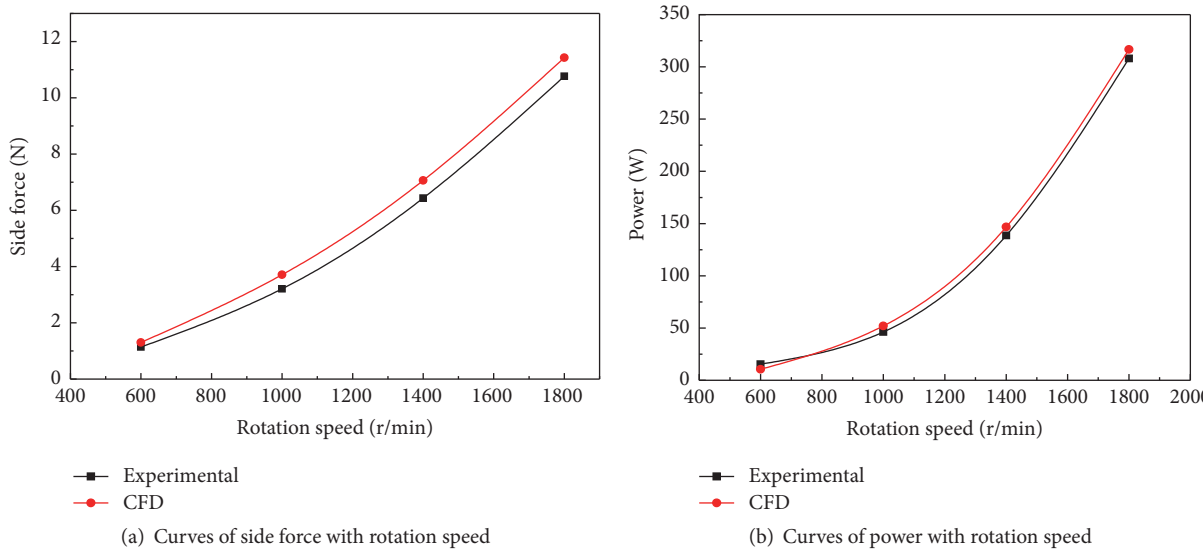

(a) Curves of side force with rotation speed

(b) Curves of power with rotation speed

Figure 11: Curves of power with rotation speed.

curve when blade number is 16, blade installation angle is 10 degrees, with interface, and opening angle is 110 degrees. We can see that there are few differences between the results of numerical simulation and the experimental results in the error range, and the tendency is consistent. This means the numerical calculation method for the side force and the required power of the reactive torque device keeps high accuracy even when blade mounting angle changes.

4.4. Hover State Comparison

4.4.1. Opening Angle Is 110 Degrees. Figure 12 shows the curves where the side force and the required power change with the rotation speed when the blade number is 12, blade mounting angle is 20 degrees, with interface, the opening angle is 110 degrees, and the collective pitch is 12 degrees. It can be seen from the figure that the numerical results are consistent with the experimental results, and the numerical method is reliable.

4.4.2. Opening Angle Changes. Test conditions are as follows: the CFF rotating speed is 1400 r/min, the blade number is 12, the blade installation angle is 20 degrees, and the rotor collective pitch is 10 degrees. Opening angle is 90 degrees, 110 degrees, 130 degrees, and 150 degrees. Figure 13 shows that the side force has an extreme point when the opening angle is between 110 degrees and 130 degrees. The power load calculated by the wind tunnel test data is 6.17 kg/kw, 6.83 kg/kw, 5.78 kg/kw, and 4.14 kg/kw with different opening angles. The antitorque device acceleration function of rotor

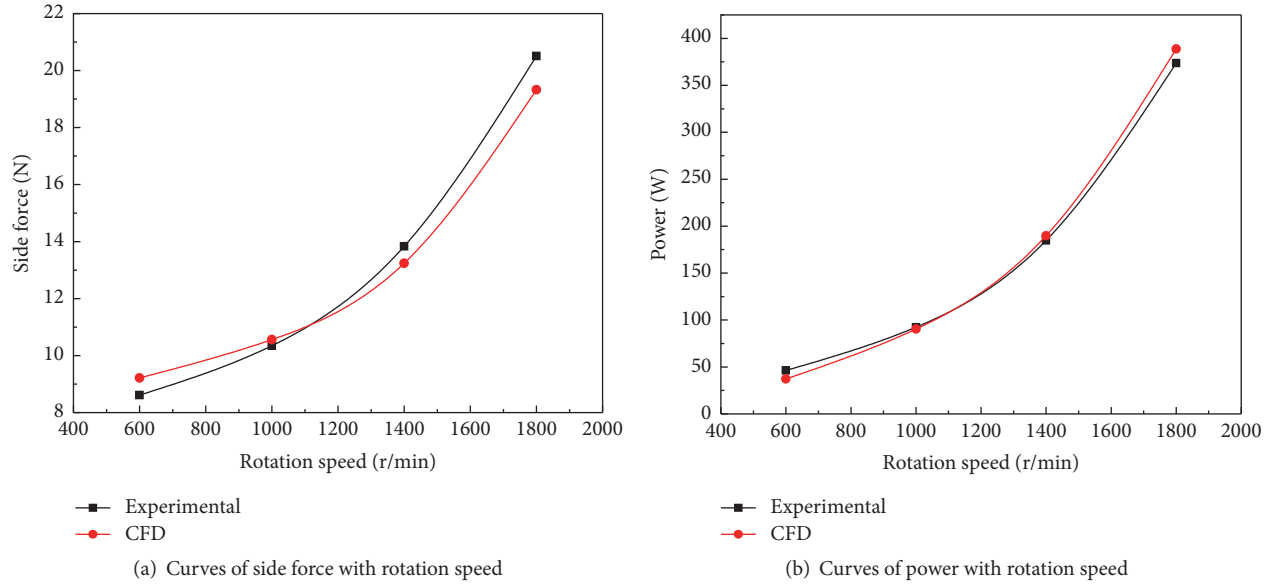

(a) Curves of side force with rotation speed (b) Curves of power with rotation speed

Figure 12: Opening angle is 110 degrees.

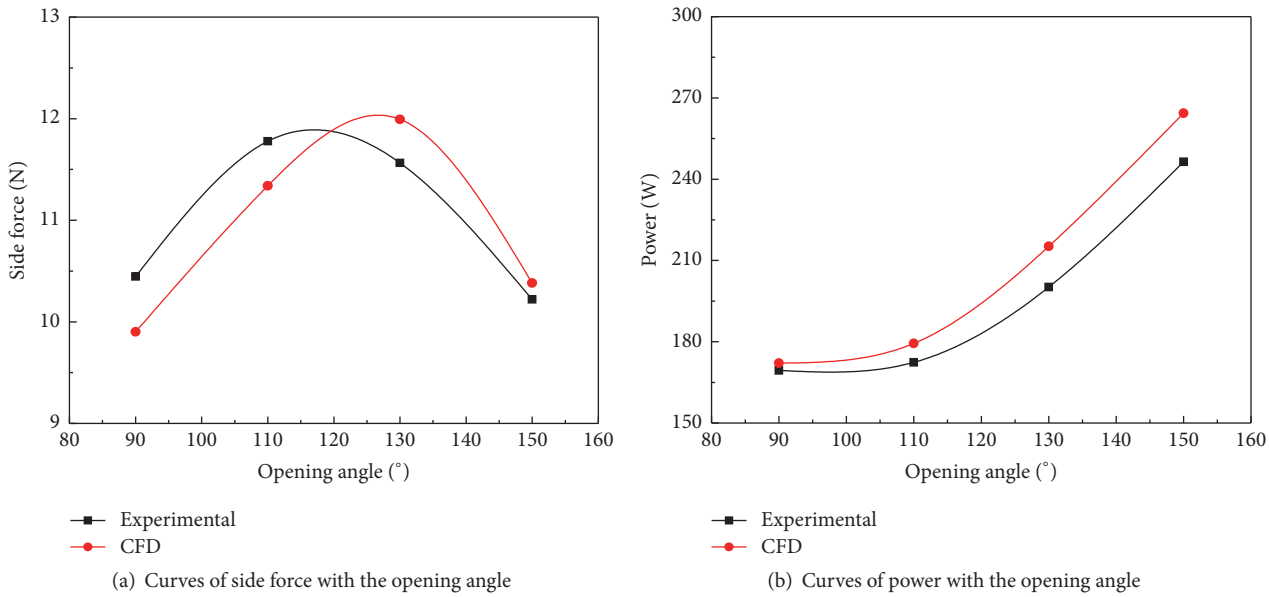

(a) Curves of side force with the opening angle (b) Curves of power with the opening angle

Figure 13: Opening angle changes.

downwash flow becomes weaker when the opening angle is larger than 110 degrees. So, a proper opening angle is also an important parameter to the antitorque device. Figure 13(a) shows the experimental and numerical calculation of side force with the antitorque device at different opening angles. The error of numerical calculation is relatively large. That is because four grid computing models need to be, respectively, built when the model of the opening angle is 90°, 110°, 130°, and 150°. The grid connection and the grid number are different between the interface and the shell, which may cause errors. However, the deviation between the calculated results and the experimental values is also acceptable.

4.4.3. Left and Right Interface Changes. The experimental conditions are as follows: rotation speed of CFF is 1400 r/min, the blade number is 12, the blade installation angle is 20 degrees, the rotor collective pitch is 10 degrees, the flow speed is 0 m/s, and the opening angle is 110 degrees. It is shown in Figure 14(a) that when the antitorque device has an interface, the side force is smaller than the other two cases and side force is larger than the other two cases with half of the interface (no left interface). Compared with the experimental data of the wind tunnel, the side force generated by the configuration is higher than that of the other two cases, which is consistent with the numerical results of this paper. By numerical simulation, it is very convenient to see

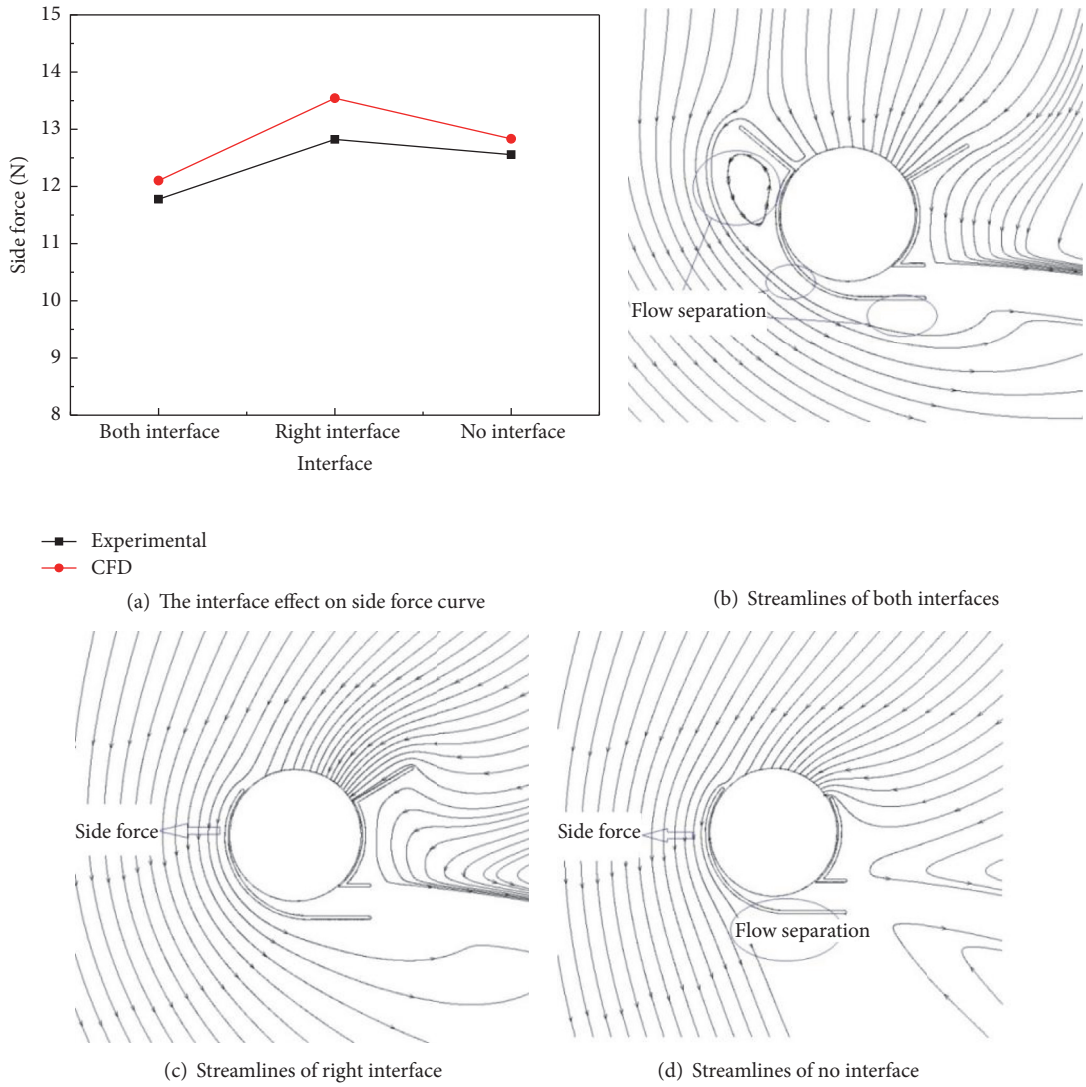

Figure 14: Left and right interface changes.

how the air flows. Figure 14(b) is the external flow field streamlines of reactive torque device with interface. It can be figured out that the location of flow separation is in the left shell of outer surface. It formed vortex near surface part of the shell and the airflow does not go along the left shell to the bottom of the shell of reactive torque device exit, but it separates from left shell. Figure 14(c) is the flow chart when reactive torque device has half interface. Figure 14(d) is the external flow chart when reactive torque device has no interface. Comparing Figure 14(c) with 14(d), we can see that the antitorque device left shell is in the rotor downwash flow and CFF suction flow, so its streamline is denser and flow speed is higher. According to the Bernoulli theorem, pressure is lower than right shell and left side force is promoted. This is favorable for reactive torque. The left shell flow characteristics of the device with right interface are similar to that with no interface. The difference is that the airflow separates later when the device has right interface. So, it can be concluded that the antitorque device produces side force by two ways. A part is that the airflow is accelerated by CFF twice, when it goes through the fan and gets ejected to the outlet. According to Newton's third law, it obtains left side force. This part of the side force accounts for about 70%. Another part of the side force is the air going through the outer surface of the antitorque device, forming velocity circulation under the effect of rotor downwash flow and CFF suction flow and producing side force which is similar to the NOTAR helicopter.

4.5. Forward Flight State Comparison

4.5.1. Forward Flight Speed Is 5 m/s. Figures 15(a) and 15(b) show the curves where the side force and the required power change with the rotation speed when the blade number is 12, blade installation angle is 20 degrees, with both interfaces, the opening angle is 110 degrees, the collective pitch is 12 degrees, and the forward speed is 5 m/s. Figure 15(a) shows the side force at different rotation speeds when forward speed is 5 m/s. The errors between numerical calculation and experimental results at 600 r/min, 1000 r/min, 1400 r/min, and 1800 r/min

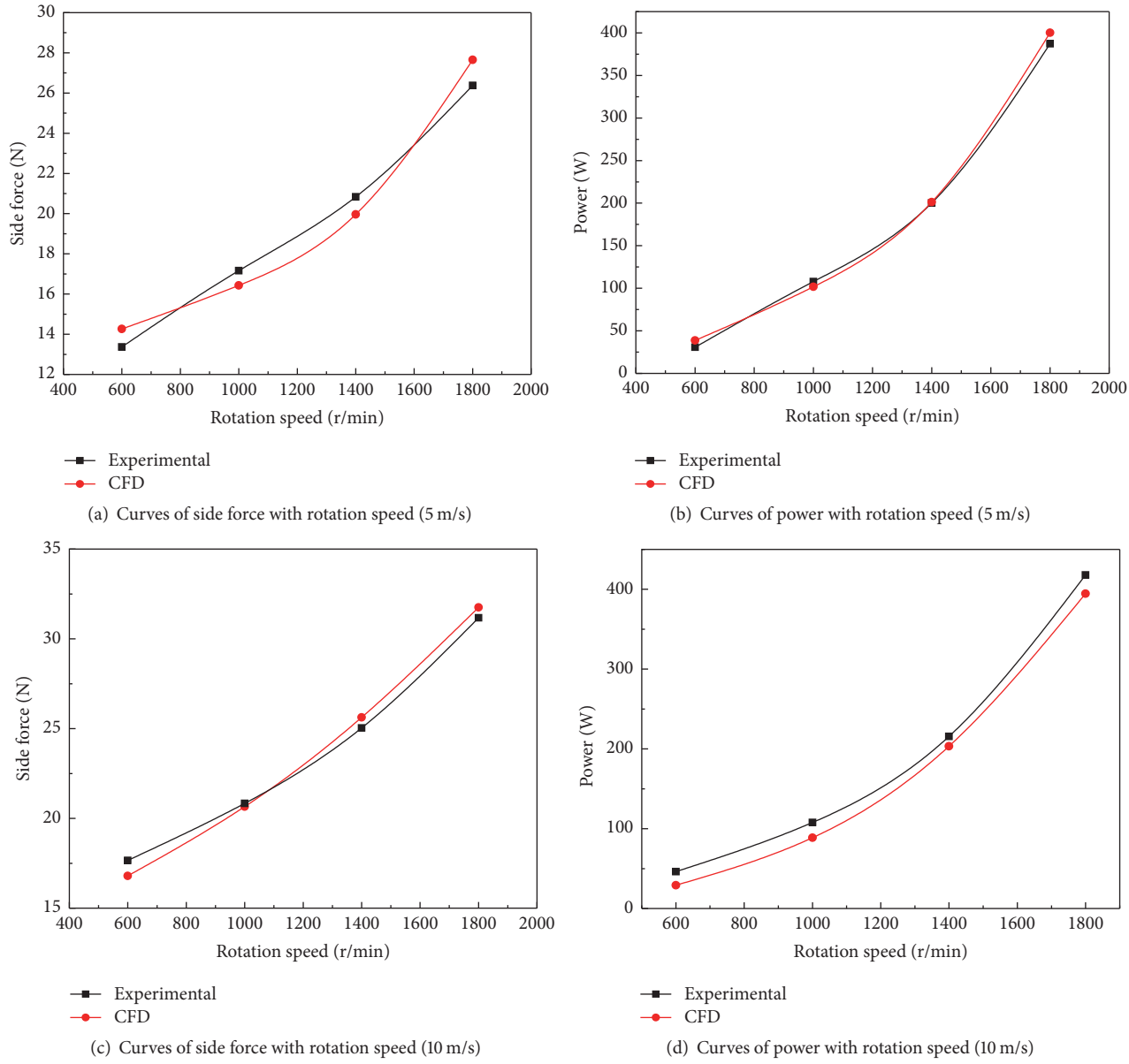

(a) Curves of side force with rotation speed (5 m/s)

(b) Curves of power with rotation speed (5 m/s)

(c) Curves of side force with rotation speed (10 m/s)

(d) Curves of power with rotation speed (10 m/s)

Figure 15: Forward flight state comparison.

are 6.7%, 4.2%, 4.1%, and 4.8%, respectively. The error is large and the experimental value is low at low speed. Probably, the eccentric vortex intensity inside the CFF is low and has not yet formed a stable pattern at low speed. And the calculated value is considered as the ideal situation; a stable flow field is formed, so the result is larger. It can be seen from the figure that the result of numerical calculation is credible.

Figures 15(c) and 15(d) show the curves where the lateral force and the required power change with the rotation speed when the blade number is 12, blade installation angle is 20 degrees, with both interfaces, the opening angle is 110 degrees, the collective pitch is 12 degrees, and the forward speed is 10 m/s. It can be seen from the figure that the results of numerical calculation are consistent with the experimental results.

5. Conclusion

The paper drew the following conclusions based on the wind tunnel test and numerical calculation method:

(1) Wind tunnel tests proved that the antitorque device can produce side force. CFF rotation speed, rotor downwash flow, and the forward flight flow have a great impact on side force. In this paper, the optimal geometric parameters for reactive torque device are as follows: the blade number is 10, with half interface, and the opening angle is 110 degrees. The test calculation power load of reactive torque device has a little difference with common helicopter and it can take place of a single-rotor helicopter tail rotor mechanism.

(2) We carried out numerical calculations at different blade installation angles, different blade numbers, different opening angles, with and without interface, different CFF rotation speeds, different rotor downwash flow speeds, different forward speeds, and compared them with the wind tunnel experiment result. Finally, this proves that the calculation result is credible.

(3) Numerical simulation flow pattern revealed initially the principle of producing side force. One part is that CFF accelerated the airflow, the other part is that the airflow bypassed the external surface of reactive torque device, formed velocity circulation, and generated the side force.

(4) According to the shape characteristic of the reactive torque device, the system can be arranged on the tail beam of the single-rotor helicopter to balance reactive torque and control course by controlling the rotation speed of the CFF.

Competing Interests

The authors declare that they have no competing interests.

Acknowledgments

The authors would like to acknowledge the financial support of the Priority Academic Program Development of Jiangsu Higher Education Institutions and the Nanjing University of Aeronautics and Astronautics Innovation Foundation (Grant no. 201501049).

References

[1] C. L. Zhang, "New developments of helicopter technology," *Journal of Nanjing University of Aeronautics and Astronautics*, vol. 29, no. 6, pp. 607–614, 1997.

[2] X. P. Ni, R. H. Cai, J. X. Cao, and J. Z. Yu, "Present situation and prospects of helicopter technology," *Acta aeronautica et Astronautica Sinica*, vol. 24, no. 1, pp. 16–20, 2003.

[3] Z.-W. Yu and Y.-H. Cao, "CFD simulation and validation of ducted tail rotor," *Journal of Aerospace Power*, vol. 21, no. 1, pp. 19–24, 2006.

[4] Y.-H. Cao, K. Chen, J. Wang, and W.-L. Yin, "CFD analysis of aerodynamic characteristics for the ducted tail rotor and its aerofoil," *Journal of Aerospace Power*, vol. 19, no. 6, pp. 792–797, 2004.

[5] S. Rao Carlo, "Tailboom design of the 520N NOTAR helicopter," in *Proceedings of the 46th Annual Forum of the American Helicopter Society, Part 1 (of 2) (AHS '90)*, vol. 1, pp. 549–556, 1990.

[6] I. Yavrucuk, H. M. Bakir, and O. Uzol, "Mathematical modeling of the NOTAR antitorque system for flight simulation," *Journal of the American Helicopter Society*, vol. 58, no. 2, Article ID 022002, pp. 407–415, 2013.

[7] J. Li and W. Yang, "An analysis of cross section of helicopter tail boom for NOTAR system," *Acta Aerodynamica Sinica*, vol. 33, no. 2, pp. 239–245, 2015.

[8] Z. X. Dong, Y. D. Gao, and H. M. Wang, "Influence of circulation control parameters on lateral thrust of helicopter tail boom in rotor downwash," *Helicopter Technique*, vol. 4, pp. 12–24, 2011.

[9] X. P. Luo, C. L. Zhang, and M. S. Shen, "No tail rotor and its experimental research," *Journal of Aerospace Power*, vol. 11, no. 1, pp. 15–18, 1996.

[10] Z. X. Dong, Y. D. Gao, and H. M. Wang, "Research on parameters of circulation control tail boom," *Aeronautical Science and Technology*, vol. 6, pp. 11–20, 2009.

[11] L. Meng, Y. Ye, and N. Li, "Research progress and application prospects of fan-wing aircraft," *Acta Aeronautica et Astronautica Sinica*, vol. 36, no. 8, pp. 2651–2661, 2015.

[12] T. Q. Dang and P. R. Bushnell, "Aerodynamics of cross-flow fans and their application to aircraft propulsion and flow control," *Progress in Aerospace Sciences*, vol. 45, no. 1–3, pp. 1–29, 2009.

[13] S. Askari and M. H. Shojaeefard, "Numerical simulation of flow over an airfoil with a cross flow fan as a lift generating member in a new aircraft model," *Aircraft Engineering and Aerospace Technology*, vol. 81, no. 1, pp. 59–64, 2009.

[14] S. Askari, M. H. Shojaeefard, and K. Goudarzi, "Experimental study of stall in an airfoil with forced airflow provided by an integrated cross-flow fan," *Proceedings of the Institution of Mechanical Engineers, Part G: Journal of Aerospace Engineering*, vol. 225, no. 1, pp. 97–104, 2011.

[15] S. Askari and M. H. Shojaeefard, "Experimental and numerical study of an airfoil in combination with a cross flow fan," *Journal of Aerospace Engineering*, vol. 227, no. 7, pp. 1173–1187, 2013.

[16] S. Askari and M. H. Shojaeefard, "Shape optimization of the airfoil comprising a cross flow fan," *Aircraft Engineering and Aerospace Technology*, vol. 81, no. 5, pp. 407–415, 2009.

[17] J. D. Kummer and T. Q. Dang, "High-lift propulsive airfoil with integrated crossflow fan," *Journal of Aircraft*, vol. 43, no. 4, pp. 1059–1068, 2006.

[18] N. Thouault, C. Breitsamter, and N. A. Adams, "Numerical and experimental analysis of a generic fan-in-wing configuration," *Journal of Aircraft*, vol. 46, no. 2, pp. 656–666, 2009.

[19] M. Tang, Z. F. Tang, and H. D. Wu, "The rotor anti-torque systems structure parameters on its aerodynamic influence," *Helicopter Technique*, vol. 2, pp. 15–19, 2013.

[20] Z. F. Tang, M. Tang, and H. D. Wu, "The analysis of the influence of rotor anti-torque system's structure parameters on its aerodynamic influence," in *Proceeding of the 2nd Asian/Australian Rotorcraft Forum and The 4th International Basic Research Conference on Rotorcraft Technology*, pp. 1–9, Tianjin, China, 2013.